Available online at www.sciencedirect.com

ScienceDirect

Journal of the European Ceramic Society 31 (2011) 1397–1403

www.elsevier.com/locate/jeurceramsoc

Porous mullite templated from hard mullite beads

E. Garcia, M.I. Osendi, P. Miranzo*

Institute of Ceramics and Glass, CSIC, Kelsen 5, Campus Cantoblanco, 28049 Madrid, Spain

Received 27 September 2010; received in revised form 18 January 2011; accepted 3 February 2011
Available online 4 March 2011

Abstract

Porous mullite bodies were developed by spark plasma sintering (SPS) amorphous mullite beads of about ~30 μm in diameter at two temperatures, 950 and 1300 °C. Materials showed a close random stacking of solid spheres that retained their original packing but slightly flattened at the contacts in some cases. Depending on the thermal history, the beads were partially or fully crystallized. The thermal conductivity of the different porous mullite materials was analyzed as a function of the microstructure. Owing to the particular porous network, high gas permeability and very low thermal conductivities (1–2 $\mathrm{W\,m^{-1}\,K^{-1}}$) were achieved, among the lowest reported for sintered mullite materials.

Keywords: Porous ceramics; Spark plasma sintering; Powder technology; Thermal properties

1. Introduction

Porous ceramics are commonly used in thermal related applications, such as molten-metal filters, high temperature thermal insulation, catalyst supports and radiant burners.[1] Recently, their functionality has been extended to other fields like energy, environment and health. Mullite is a suitable material for some of these applications as it combines high temperature strength, creep resistance, high corrosion resistance and low thermal conductivity.[2,3] Although many works deal with the processing of mullite bodies[4–10] with porosities ≥30%, there is just one work[3] studying its thermal conductivity as a function of porosity (up to 60 vol%). In that case, pores were rounded with sizes in the range 20–50 μm, patterned from starch granules, enclosed in a continuous mullite matrix, and the thermal behavior fitted Eucken's model[11] for biphasic materials, with thermal conductivity ranging from 1 to 2.5 $\mathrm{W\,m^{-1}\,K^{-1}}$. Even lower thermal conductivities can be expected if mullite materials with connected pores were achieved. In present work, we develop porous mullite bodies formed by stacking solid, quasi-amorphous or crystalline mullite spheres, that is, the carbon copy of the above starch-based porous mullite. These porous mullites have a very low thermal conductivity, lower than the starch-based porous mullite of similar porosity level.

The fabrication process of quasi-amorphous mullite spheres has been studied in a previous work of the present authors.[12] It was proved that flame spraying of mullite powders led to beads with very low crystallinity ratio (0.11–0.19, depending on the starting mullite powders) that became completely crystalline when treated at 1300 °C. In that work, the formation of the pseudo-tetragonal mullite was observed for beads treated at 1000 °C.

Among the different sintering techniques, the spark plasma sintering (SPS), which is a pressure assisted pulsed direct current sintering method, allows much faster heating rates and shorter sintering times, together with commonly lower sintering temperatures, compared to conventional sintering methods, such as pressureless sintering, hot pressing or hot isostatic pressing.[13–15] This technique extraordinarily enhances the sinterability of most of the materials and extends the possibilities for developing new advanced materials with tailored properties. For that reason, SPS has been selected for sintering the stacked mullite beads at temperatures as low as 950 °C using short holding times of 5 min, which will allow maintaining the initial stacking geometry and some of the amorphous and transitory phases in the starting beads.

2. Experimental

Two different mullite ($3Al_2O_3{\cdot}2SiO_2$) powders were used: (i) SiO_2–Al_2O_3 granulated gel powders with a bohemite-like struc-

---

* Corresponding author.
E-mail address: pmiranzo@icv.csic.es (P. Miranzo).

0955-2219/$ – see front matter © 2011 Elsevier Ltd. All rights reserved.
doi:10.1016/j.jeurceramsoc.2011.02.004

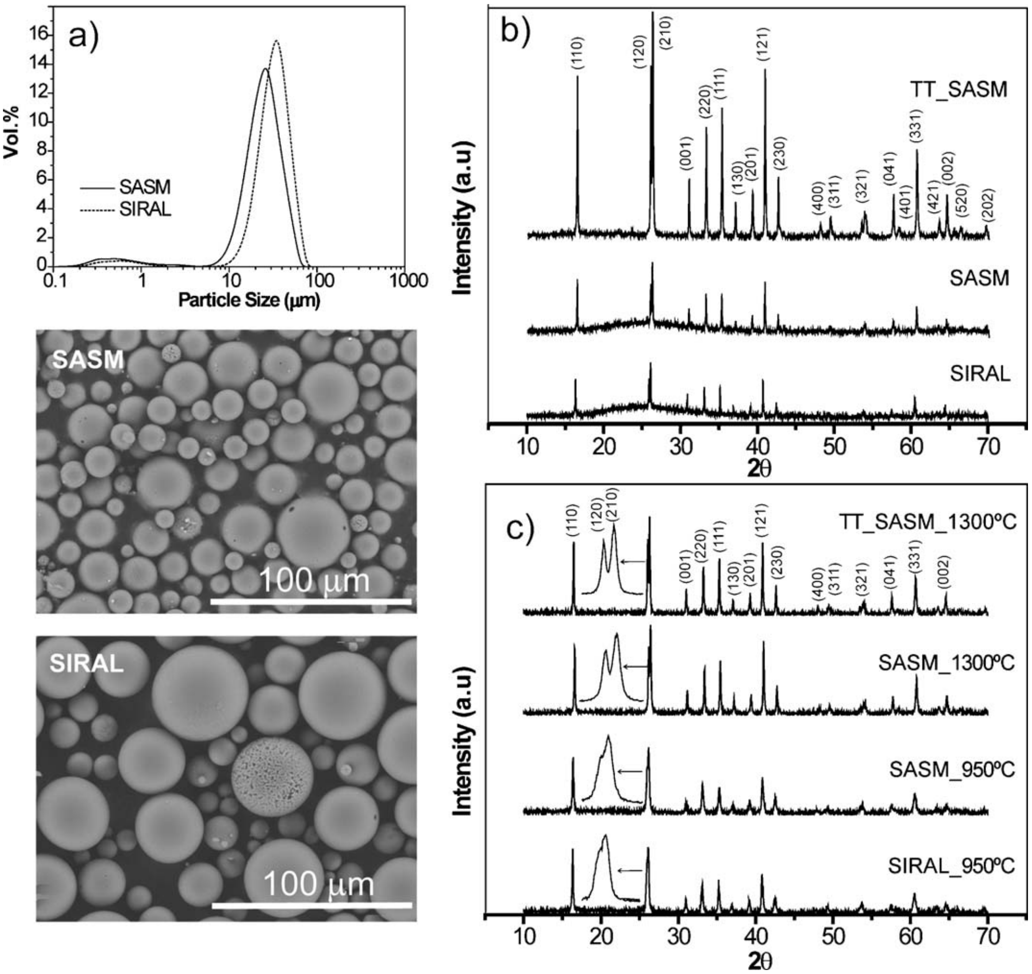

Fig. 1. Particle size distributions and SEM micrographs of the mullite beads obtained by flame spraying (a), XRD patterns of the different starting beads (b) and the SPS specimens (c).

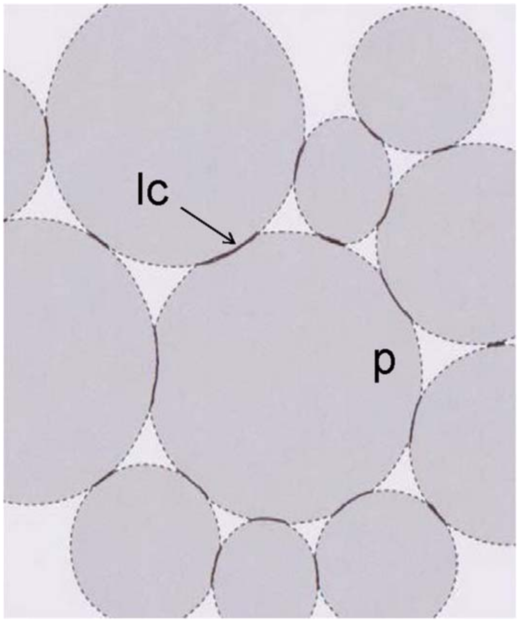

Fig. 2. Scheme of a cross section of the sintered materials showing parameters used for *f* calculation: *lc* is the contact length and *p* the sphere perimeter.

ture (SIRAL 28 M, Condea C, Germany) and mean particle size (d_{50}) of ~41 μm and (ii) crystalline mullite powders (Baikalox SASM, Baikowski Chemie, France) having d_{50} = 1.3 μm. Aqueous suspensions of SASM powders (30 wt% of solid contents) were spray dried to get granules of ~26 μm, slightly smaller than the SIRAL gel.

Both granulated powders were flame sprayed into a water filled metal container using an oxygen–acetylene gun. The temperature and velocity of the particles were measured with the Accuraspray-g3 sensing system (Tecnar Automation Ltd., St. Bruno, QC, Canada) obtaining velocities of 80 m s^{-1} and temperatures of 3100 °C, high enough for melting the mullite powders. Afterwards, the beads were drained, dried at 120 °C and sieved discarding agglomerates above 63 μm. Beads flame sprayed from gel-type powders had bigger sizes (d_{50} = 30.0 μm) than those from SAMS powders (d_{50} = 22.5 μm), as seen in Fig. 1a, accordingly to the differences in their initial agglomerate sizes. A batch of the SASM beads was furnace treated (TT_SAMS) at 1300 °C for 1 h to improve their crystalinity before sintering. In this way, fully crystalline beads were obtained (Fig. 1b).

Disc shaped specimens of 20 mm in diameter and 3 mm in thickness were obtained from the different beads (as-sprayed

Table 1
Apparent ($\rho_{app.}$), bulk (ρ_{bulk}) and theoretical ($\rho_{theor.}$) densities, open (Φ_{Open}) and total (Φ_{Total}) porosities, and crystallinity ratio normalized to the 1300 °C fully crystallized specimens (CR_N).

Material	ρ_{app} (g cm^{-3})	ρ_{bulk} (g cm^{-3})	$\rho_{theor.}$ (g cm^{-3})	Φ_{Open}	Φ_{Total}	CR_N
SIRAL_950	2.95	2.38	3.06	0.19	0.22	0.87
SASM_950	2.99	2.43	3.06	0.19	0.21	0.88
SASM_1300	3.03	2.64	3.15	0.13	0.16	0.97
TT_SASM_1300	2.87	1.99	3.16	0.31	0.37	1

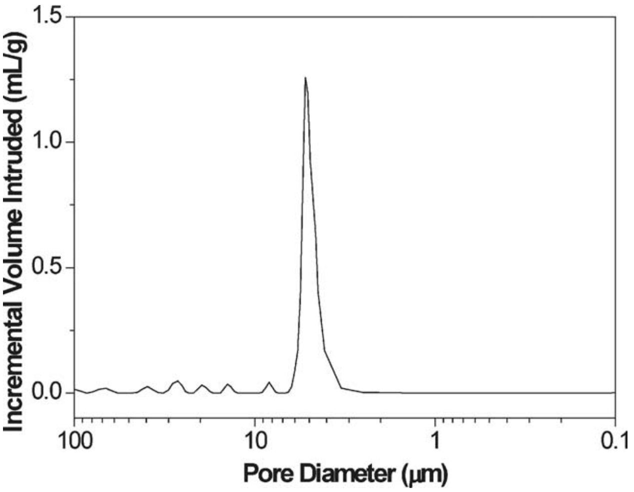

Fig. 3. Plot of the intruded volume of mercury versus pore diameter of the TT_SASM_1300 sample.

and TT) by spark plasma sintering (Dr. Sinter 510CE, SPS Syntex Inc., Japan) at two temperatures, 950 and 1300 °C, for 5 min applying 40 MPa of uniaxial pressure and vacuum atmosphere (labels for each sample are shown in Table 1). Heating and cooling rates were 75 and 120 °C min^{-1}, respectively. Ram displacement was continuously recorded during sintering runs. The apparent densities and the open porosities of the specimens were measured by the Archimedes' method using the boiling water penetration method (specimens were immersed in boiling water for 30 min and then kept in water for 18 h).

The pore size distribution of the samples was measured by mercury intrusion porosimetry (Poremaster®, Quanchrome instruments, USA). The maximum injection pressure was about 200 MPa. The Hg contact angle and surface tension used for the calculations were 140° and 480 × 10^{-3} N m^{-1}, respectively.

Samples of 1 mm thickness and 12.7 mm in diameter were used for permeability measurements. Specimens were butted into a Cu cylindrical cell sealing the periphery and connecting both sides of the cell to the gas tubes to force the gas flowing

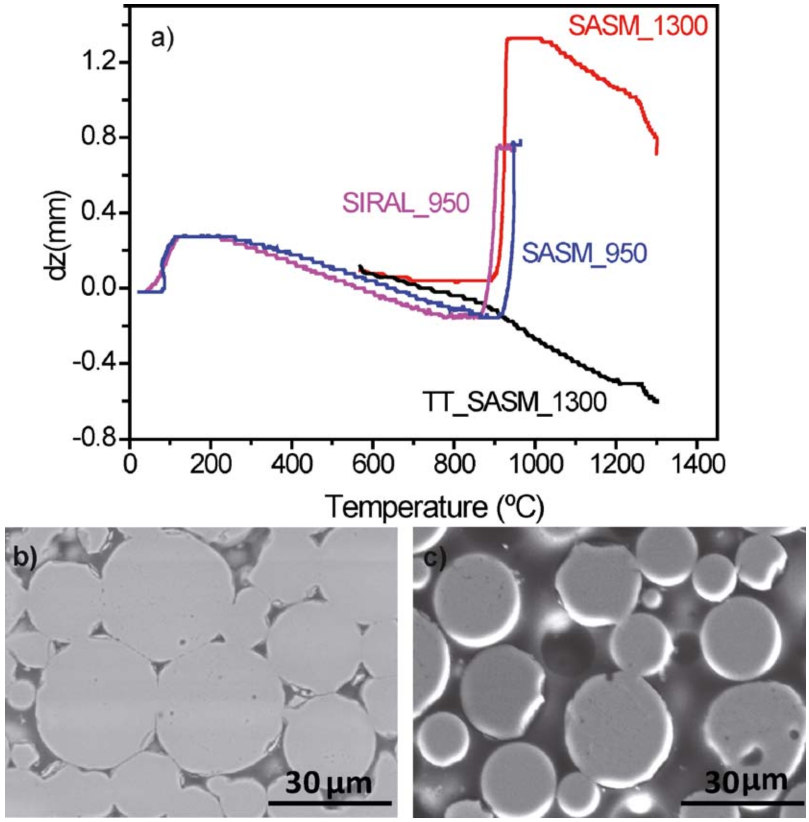

Fig. 4. Piston displacement versus temperature for the different SPS runs and cross-section views of (a) SASM_1300 and (b) TT_1300_SASM specimens.

Table 2
Fraction of solid contacts between beads (*f*), ratio of contact radius to sphere radius (γ), measured effective thermal conductivity ($K_{eff.}$) at room temperature (RT), calculated reduced thermal conductivity (K_{eff}/K_0) and solid phase thermal conductivity (K_0) deduced from K_{eff} and K_{eff}/K_0.

Material	f	γ	K_{eff} (RT) (W m^{-1} K^{-1})	K_{eff}/K_0 (RT) (W m^{-1} K^{-1}) Siu and Lee[28]	K_0 (RT) (W m^{-1} K^{-1})
SIRAL_950	0.34	0.68	1.36	0.56	2.43
SASM_950	0.34	0.68	1.37	0.56	2.45
SASM_1300	0.38	0.76	1.99	0.63	3.16
TT_SASM_1300	0.18	0.36	1.19	0.30	3.97

through the specimen, at a given flow rate.[16] The gas permeability of the porous mullites was evaluated using the equation:

$$\Delta P = \frac{\eta L}{\mu A} Q \tag{1}$$

where ΔP is the pressure drop across the specimen, μ is the Darcy's permeability, η is the dynamic viscosity of the fluid (in this case, that of nitrogen: 1.75×10^{-5} Pa s),[17] A and L are the cross-sectional area and the thickness of the sample, respectively, and Q is the flow rate.

X-ray diffraction patterns (XRD, Xpert PRO, PANalytical, Netherlands) of beads and powdered SPS specimens were recorded using a $\theta/2\theta$ configuration. The microstructure of beads and sintered samples were observed by Scanning Electron Microscopy (FE-SEM, Hitachi 4700, Japan). The fraction of solid contacts between beads (*f*), defined as the ratio between total contact length ($\sum lc_i$) and total particles perimeter ($\sum p_i$) (see Fig. 2), was quantitatively measured on polished specimens using image analysis software on SEM images of ~200 μm × 200 μm, containing at least 400 features. From this analysis the ratio of contact radius to sphere radius ($\gamma = r_c/r_s$) as well as the number of contacts per sphere ($N = N_c/N_s$) was also estimated. The 3D mean sphere radius r_s was estimated dividing by 0.785 the 2D mean sphere radius as proposed by Kong et al.[18]

The thermal diffusivity (α) was measured by the laser flash method (Thermaflash 2200, Holometrix/Netzsch USA). Disk shaped samples of 12.7 mm in diameter and ~1 mm in thickness were tested up to 800 °C in Ar atmosphere. Disk surfaces were gold and graphite coated to enhance absorption of the laser beam. Thermal conductivity (K) was calculated from specific heat (C_p) of mullite[19] and density (ρ) using the expression $K = \alpha \cdot \rho \cdot C_p$. Surface roughness was <50 μm and then thickness correction was not necessary[20] as it gave variability within the 5% accuracy range of the technique.

3. Results and discussion

As-sprayed beads were mainly amorphous with some traces of mullite, as the presence of a broad hump in the XRD patterns at ~26° (2θ) reveals (Fig. 1b). Amorphization was a consequence of the high flame spraying temperature (3100 °C), which is above the melting point of mullite (~1860 °C).[2] Due to its incongruent melting and to the rapid cooling, bulk crystallization in the beads did not occur.[12] Extensive mullite crystallization was observed only after heating, either in the TT_SASM beads or in the SPS specimens (Fig. 1c). XRD spectra of the sintered samples showed overlapping of the (1 2 0) and (2 1 0) mullite peaks at ~26° (2θ) for the 950 °C specimens (inserts in Fig. 1c), indicating the formation of the so-called pseudotetragonal mullite.[21] For the 1300 °C SPS specimens, peaks split apart evidencing the formation of the orthorhombic mullite, and similarly for the TT_SAMS beads, heat treated at 1300 °C. An estimation of residual amorphous phase in the mullite specimens was obtained from the crystallinity ratio (CR_N), defined as the ratio between the area under the XRD peaks and the area under the whole pattern, normalized to the 1300 °C fully crystallized specimens,[12] giving around 10 wt% of amorphous phase in the case of the 950 °C specimens (Table 1).

The porosity of the specimens was estimated from the ratio between the experimentally measured bulk density and the theoretical density (see Table 1), which was calculated from the rule of mixtures using the following expression:

$$\rho_{th} = x_a \cdot \rho_a + x_c \cdot \rho_c \tag{2}$$

where x is the volume fraction and ρ is the density of amorphous (a) and crystalline (c) phases. The density measured by helium pycnometry for the mainly amorphous as-sprayed beads (2.85 g cm^{-3}) was used as ρ_a. According to phases detected in the XRD patterns of specimens sintered at 950 and 1300 °C (Fig. 1c), the density of the pseudo-tetragonal (3.09 g cm^{-3}) and the orthorhombic (3.16 g cm^{-3}) mullites[21] were respectively used for ρ_c in Eq. (2). In this way, the theoretical density changed from 3.06 g cm^{-3} for the 950 °C specimens to 3.16 g cm^{-3} for the 1300 °C specimens and porosities of the materials varied then from 16 to 37% (Table 1), depending on the sintering temperature and the beads crystallinity; open porosity varied between 13 and 31% and intra-bead porosity fluctuated from 2 to 6%. Intruded volume of mercury versus pore diameter curves (Fig. 3) were very similar for all SPS porous mullites, showing a narrow pore size distribution (3–10 μm) centered at ~5.3 μm.

The most remarkable feature of the SPS displacement curves (Fig. 4) was that, except for the mullite processed from the crystalline beads, a sudden contraction occurred at about 900 °C. This effect can be explained considering the amorphous nature of the as-sprayed beads that allowed deformation during SPS by the simultaneous effects of temperature and load, leading to contact flattening as it is shown in Fig. 4b. Additionally, the crystallization process may also contribute to the sudden shrinkage as density of the crystalline mullite is higher than that of amorphous mullite. Conversely, the crystalline TT beads did not deform under same conditions, keeping instead the regular spherical shape of the original beads (Fig. 4c). Accordingly the TT beads SPS at 1300 °C showed the lowest density among the specimens (Table 1), being slightly higher (69%) than the

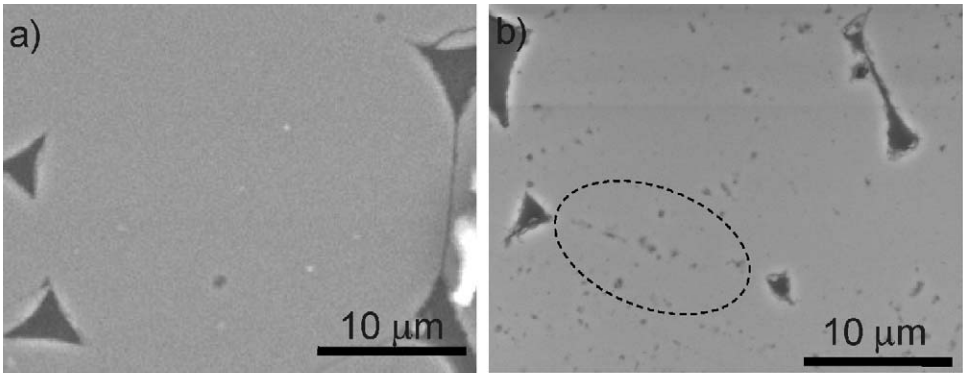

Fig. 5. Detail of the beads in SASM_950 (a) SASM_1300 (b). A flawed interface area is enclosed by a dashed line.

density of close random packed monodispersed spheres (64%). When amorphous beads were used, density increased with SPS temperature and it did not depend on the type of starting mullite powders (SASM or SIRAL) (Table 1).

As seen in the SEM micrographs of Fig. 4, the high sintering rates of SPS allowed developing inter-bead sinter necks at temperatures as low as 950 °C while maintaining the initial structure of stacked beads. Specimens sintered at 950 °C containing pseudotetragonal mullite (Fig. 1c) showed minute crystallites within the beads (Fig. 5a), whereas those sintered at 1300 °C, formed mainly by orthorhombic mullite (Fig. 1c), exhibited intra-bead microporosity (Fig. 5b). This agrees with data[21] reporting that mullite melts crystallizing below 1200 °C into pseudo-tetragonal mullite and SiO_2 rich inclusions have lower density than the 1300 °C orthorhombic mullite. A simple calculation predicts intra-bead porosity fraction of 0.06 for the 1300 °C specimens, considering changes in density from the pseudo-tetragonal to the orthorhombic mullites, which is quite similar to the values calculated from porosity data in Table 1 0.03–0.06.

The N_2 permeability measured for the SASM_950 and TT_SASM_1300 materials, both with porosity above 20%, gave values of 1.5×10^{-17} and $1.1 \times 10^{-16}\,m^2$, respectively. Therefore, increasing porosity from 21 to 37% augmented the permeability by one order of magnitude. Furthermore, mullite beads sintered at 950 °C showed permeation at much lower porosity than predicted from the percolation model (0.31).[22] As it is shown in Fig. 6, materials from beads present lower permeability values than porous ceramics processed by extrusion but higher than ceramics processed by conventional routes, which also show permeation at higher porosity fractions.[23]

The K of the porous mullite bodies (Fig. 7) was almost constant with temperature and had values 60–75% lower than the values for dense SASM mullite.[3] No significant differences between the specimens sintered at 950 °C were observed, whereas specimen sintered at 1300 °C from amorphous beads showed much higher K values (>40%), quite similar to those measured for a mullite processed from starch with 36 vol% of porosity,[3] as seen in Fig. 7, although the later material had more porosity and its thermal conductivity slightly decreased with temperature. Conversely, very low K values were measured for the TT SASM 1300 specimen.

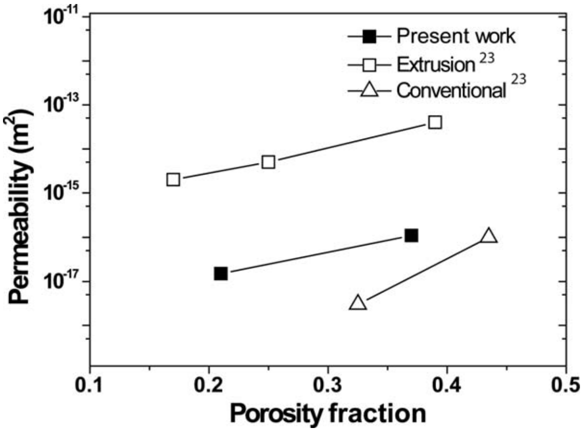

Fig. 6. Relationships between porosity and permeability of porous ceramics prepared in the present work compared with materials obtained by extrusion and conventional methods.[23]

Effective medium models like the power-law and the exponential models,[24–26] predict higher thermal conductivity values ($2.5–3.8\,W\,m^{-1}\,K^{-1}$) than those experimentally measured. Therefore, the porosity dependence of thermal conductivity for materials with *partially sintered* microstructures cannot be

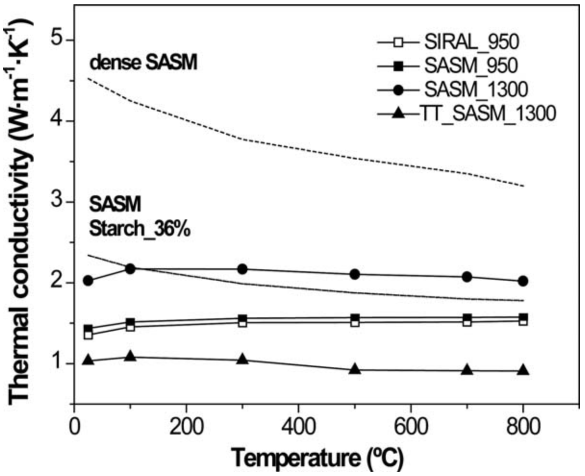

Fig. 7. Thermal conductivity as a function of temperature for the SPS porous mullites. Values for dense and porous SASM mullite (36 vol% porosity) prepared from starch addition[3] are also plotted (discontinuous lines).

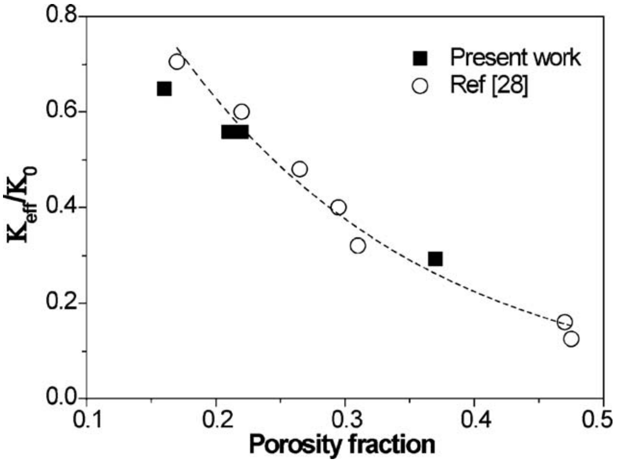

Fig. 8. K_{eff}/K_0 values at room temperature as a function of porosity for the SPS specimens (full symbols) and the values calculated by Siu and Lee[28] (empty symbols).

described by the otherwise quite realistic previous models but more sophisticated models should be used. Different methods have been proposed for calculating the effective thermal conductivity (K_{eff}) of porous materials formed by spherical particles with different types of packing.[27–31] Siu and Lee[28] developed a method to calculate the effective thermal conductivity of packed beds considering structured stacks, which was validated for porosities between 0.5 and 0.2 by comparison with experimental data from the literature, and where the conductivity of the solid phase was much larger than that of the surrounding fluid matrix. They considered that randomly packed beds were based on three different ordered structures, depending on porosity, i.e. a simple cubic (SC), body-centre cubic (BCC) or face centre cubic (FCC) packing. They proposed a dependence of the reduced thermal conductivity, K_{eff}/K_0, to the contact radius to sphere radius ratio, γ:

$$\frac{K_{eff}}{K_0} = A \cdot \gamma \tag{3}$$

where A varied from 0.827 to 2.421 depending on the packing geometry. Similar prediction was made by Gusarov et al.[29] but with slightly larger A values (1–2.828). In our case, it can be assumed a simple cubic packing as the average number of contacts per sphere was $N = 1.24 \pm 0.18$, calculated by image analysis on the cross-sections of the specimens. However, very large values of solid contact fractions and contact radius to sphere radius were measured in the present case (Table 2), the increasing f and γ figures being related with a progressive flattening of the inter-particle necks during sintering by SPS while maintaining the packing geometry. Accordingly, a value of $A = 0.827$ (simple cubic geometry) was used in Eq. (3) to deduce the K_{eff}/K_0 values shown in Table 2. In Fig. 8, those K_{eff}/K_0 figures are plotted versus porosity fraction together with values calculated by Siu and Lee[28] for different cubic stacking of spheres. As K_{eff}/K_0 deduced from Eq. (3) fits simulations, cubic packing seems to correctly describe the thermal behavior of the present materials.

Furthermore, K_0 of the solid phase can be estimated using the calculated K_{eff}/K_0 values. As seen in Table 2, the value for the TT_SASM_1300 material (3.97 W m^{-1} K^{-1}), which was sintered at 1300 °C from crystalline beads, is close to that of dense crystalline mullite (Fig. 7) corrected using the Eucken's equation for an intra-bead porosity fraction of 0.06 (4.4 W m^{-1} K^{-1}). However, K_0 values are significant lower in the case of porous mullite processed from amorphous beads. As it is explained below, these low values may be due to the presence of either thermal resistances at the inter-particle contacts or the nature of pseudo-tetragonal mullite, both contributing to decreasing the effective thermal conductivity.

Due to orthorhombic mullite crystallization from amorphous or pseudo-tetragonal mullite, flawed contacts between particles formed, as those shown in Fig. 5, in compacts sintered at 1300 °C from amorphous beads. These imperfect interfaces would act as thermal barriers for heat flow with a considerable reduction in the effective thermal conductivity, as interface roughness governs the effective thermal contact area.[31] This would explain that K_0 deduced for SASM_1300 mullite (Table 2) were 20% lower than that deduced for the TT_SASM_1300 material.

On the other hand, microporosity was not detected in materials sintered at 950 °C but pseudo-tetragonal mullite was the major phase in this case (see Fig. 1c) that has higher Al_2O_3 content and associated oxygen vacancies compared to orthorhombic mullite[32] and, accordingly, it should have lower intrinsic thermal conductivity. In fact, a very low K_0 value (2.43 W m^{-1} K^{-1}) was estimated for the solid-phase in the materials sintered at 950 °C. Considering that these materials contain 10 wt% of amorphous phase that should have similar thermal conductivity as fused silica (1 W m^{-1} K^{-1})[33] a value of 2.65 W m^{-1} K^{-1} can be predicted for the pseudo-tetragonal mullite using Eucken's model being in close agreement with the obtained K_0 value.

4. Conclusions

Partially crystalline porous mullite materials have been developed from mullite beads using the spark plasma sintering. The sintering behavior of mullite beads prepared by flame spraying does not depend on the starting mullite powders but on their crystallinity. Amorphous beads deform during sintering at temperatures below the crystallization onset (~950 °C), enhancing densification by contact flattening. Their microstructure can be described as a solid network of beads of ~30 μm in diameter embedded in a web of channels (pores). Owing to this particular pore distribution, high gas permeability (up to 1.1×10^{-16} m^2) and very low thermal conductivity values were achieved (1–2 W m^{-1} K^{-1}) for relatively low porosities. The thermal conductivity is explained by simulations for simple cubic stacking of spheres. The predicted effective thermal conductivity of the solid phase is lower than that of crystalline mullite due to the presence of either thermal resistances at the inter-particle contacts, in the case of materials sintered at 1300 °C, or pseudo-tetragonal mullite with lower thermal conductivity than orthorhombic phase, for materials sintered at 950 °C.

Acknowledgements

Supported by CSIC (Spain) (project 2007CA003) and the Ministry of Science and Innovation (Spain) (projects MAT2006-07118 and MAT2009-09600). Eugenio Garcia acknowledges the Ramón y Cajal Program for his financial support.

References

1. Sheppard LM. Porous materials. In: Ishizaki K, Sheppard LM, Okada S, Hamasaki T, Huybretzhts B, editors. *Ceramic transactions*, vol. 31. Westerville, OH: Amer. Ceram. Soc.; 1993. p. 3–23.
2. Schneider H, Okada K, Pask JA. *Mullite and mullite ceramics*. NY: John Wiley & Sons; 1994.
3. Barea R, Osendi MI, Ferreira JMF, Miranzo P. Thermal conductivity of highly porous mullite material. *Acta Mater* 2005;**53**:3313–8.
4. Abe H, Seki H, Fukunaga A, Egashira M. Preparation of bimodal porous mullite ceramics. *J Mater Sci* 1994;**29**:1222–6.
5. Miao X. Porous mullite ceramics from natural topaz. *Mater Lett* 1999;**38**:167–72.
6. Atisivan R, Bose S, Bandyopadhyay A. Porous mullite preforms via fused deposition. *J Am Ceram Soc* 2001;**84**:221–4.
7. Liu YF, Liu XQ, Wei H, Meng GY. Porous mullite ceramics from national clay produced by gelcasting. *Ceram Int* 2001;**27**:1–7.
8. She JH, Ohji T. Fabrication and characterization of highly porous mullite ceramics. *Mater Chem Phys* 2003;**80**:610–4.
9. Barea R, Osendi MI, Ferreira JMF, Miranzo P. Fabrication of highly porous mullite materials. *J Am Ceram Soc* 2005;**88**:777–9.
10. Ding SQ, Zeng YP, Jiang DL. Fabrication of mullite ceramics with ultrahigh porosity by gel freeze drying. *J Am Ceram Soc* 2007;**90**: 2276–9.
11. Kingery WD, Bowen HK, Uhlmann DR. *Introduction to ceramics*. 2nd ed. New York (NY): John Wiley & Sons; 1976.
12. Garcia E, Mesquita-Guimarães J, Miranzo P, Osendi MI. Crystallization studies in mullite and mullite-YSZ beads. *J Eur Ceram Soc* 2010;**30**:2003–8.
13. Munir ZA, Anselmi-Tamburini U, Ohyanagi M. The effect of electric field and pressure on the synthesis and consolidation of materials: a review of the spark plasma sintering method. *J Mater Sci* 2006;**41**: 763–77.
14. Orru R, Licheri R, Locci AM, Cincotti A, Cao G. Consolidation/synthesis of materials by electric current activated/assisted sintering. *Mater Sci Eng Rep* 2009;**63**:127–287.
15. Belmonte M, González-Julián J, Miranzo P, Osendi MI. Spark plasma sintering: a powerful tool to develop new silicon nitride-based materials. *J Eur Ceram Soc* 2010;**30**:2937–46.
16. Conesa A, Fernández Roura A, Pitarch JA, Vicente-Mingarro I, Rodríguez MA. Separation of binary gas mixtures by means of sol–gel modified ceramic membranes. Prediction of membrane performance. *J Membr Sci* 1999;**155**:123–31.
17. McCarty RD, Haynes WM, Hanley HJM. The viscosity and thermal conductivity coefficients of dilute nitrogen and oxygen. *J Phys Chem Ref Data* 1974;**3**:979–1018.
18. Kong M, Bhattacharya RN, James C, Basu A. A statistical approach to estimate the 3D size distribution of spheres from 2D size distributions. *GSA Bull* 2005;**117**:244–9.
19. Hildmann B, Schneider H. Heat capacity of mullite: new data and evidence for a high-temperature phase transformation. *J Am Ceram Soc* 2004;**87**:227–34.
20. Garcia E, Osendi MI, Miranzo P. Thermal diffusivity of porous cordierite ceramic burners. *J Appl Phys* 2002;**92**:2346–9.
21. Johnson BR, Kriven WM, Schneider J. Crystal structure development during devitrification of quenched mullite. *J Eur Ceram Soc* 2001;**21**:2541–62.
22. Jan N. Large lattice random site percolation. *Physica A* 1999;**266**:72–5.
23. Isobe T, Kameshima Y, Nakajima A, Okada K, Hotta Y. Gas permeability and mechanical properties of porous alumina ceramics with unidirectionally aligned pores. *J Eur Ceram Soc* 2007;**27**:53–9.
24. Pabst W, Gregorova E. A new percolation-threshold relation for the porosity dependence of thermal conductivity. *Ceram Int* 2006;**32**:89–91.
25. Pabst W, Gregorová E, Tichá G. Effective properties of suspensions, composites and porous materials. *J Eur Ceram Soc* 2007;**27**:479–82.
26. Zivcová Z, Gregorová E, Pabst W, Smith DS, Michot A, Poulier C. Thermal conductivity of porous alumina ceramics prepared using starch as a pore-forming agent. *J Eur Ceram Soc* 2009;**29**:347–53.
27. Singh KJ, Singh R, Chaudhary DR. Heat conduction and a porosity correction term for spherical and cubic particles in a simple cubic packing. *J Phys D: Appl Phys* 1998;**31**:1681–7.
28. Siu WWM, Lee SHK. Effective conductivity computation of a packed bed using constriction resistance and contact angle effects. *Int J Heat Mass Transfer* 2004;**43**:3917–24.
29. Gusarov AV, Laoui T, Froyen L, Titov VI. Contact thermal conductivity of a powder bed in selective laser sintering. *Int J Heat Mass Transfer* 2003;**46**:1103–9.
30. Taguchi I, Kurashige M. Microstructures and macroscopic conductivity of randomly packed and uniaxially pressed sphere compacts. *Int J Heat Mass Transfer* 2007;**50**:3809–19.
31. Slavin AJ, Londry FA, Harrison J. A new model for the effective thermal conductivity of packed beds of solid spheroids: alumina in helium between 100 and 500 °C. *Int J Heat Mass Transfer* 2000;**43**:2059–73.
32. Schneider H, Schreuer J, Hildmann B. Structure and properties of mullite – a review. *J Eur Ceram Soc* 2008;**28**:329–44.
33. Cahill DG, Watson SK, Pohl RO. Lower limit to the thermal conductivity of disordered crystals. *Phys Rev B* 1992;**46**:6131–40.